IOSR Journal of Applied Chemistry (IOSR-JAC)
e-ISSN: 2278-5736.Volume 19, Issue 6 Ser. I (June. 2026), PP 58-76
www.iosrjournals.org

Green Nanotechnology Approach to Iron(II) Clathrochelate-Based Anticancer Nanoplatforms

Dr. Vikash Kumar
Assistant Professor
PG Department of Chemistry, Rajendra College, Chapra, Bihar, India

Abstract: *Iron(II) clathrochelates, a class of cage-type coordination compounds in which a metal ion is encapsulated within a macrobicyclic tris-dioximate ligand framework, have emerged as promising candidates for anticancer therapy owing to their structural rigidity, tuneable redox activity, and capacity for selective biomolecular interactions. However, conventional synthesis of these complexes and their nanoformulations often relies on hazardous organic solvents, energy-intensive conditions, and toxic reducing agents, raising significant environmental and biocompatibility concerns. This chapter presents a systematic investigation of green nanotechnology approaches for the fabrication of iron(II) clathrochelate-based anticancer nanoplatforms. The coordination chemistry of clathrochelate cage formation is first established, and the relevant thermodynamic and kinetic parameters governing template self-assembly are formulated. Green synthesis methodologies—employing plant-derived phytochemicals, biopolymeric stabilizers, and aqueous-phase processing—are described as environmentally benign alternatives to conventional routes. Characterization techniques including UV-Vis spectroscopy, dynamic light scattering, transmission electron microscopy, and X-ray diffraction are employed to validate nanoplatform formation. The chapter presents detailed results on cytotoxicity against selected cancer cell lines, cellular uptake mechanisms, and reactive oxygen species generation. Finally, the therapeutic results are discussed in the context of targeted drug delivery, tumour microenvironment responsiveness, and translational potential, along with a critical assessment of the limitations of the current green synthesis framework.*

Keywords: *Iron(II) clathrochelates, Green nanotechnology, Anticancer nanoplatforms, Cage complexes, Phytochemical synthesis, Reactive oxygen species, Cytotoxicity, Targeted drug delivery.*

Date of Submission: 15-06-2026 Date of Acceptance: 28-06-2026

I. Introduction

Nanotechnology has fundamentally transformed the landscape of cancer therapeutics by enabling the design of drug delivery systems with unprecedented control over size, morphology, surface chemistry, and pharmacokinetic behaviour [1, 2]. Conventional chemotherapeutic agents suffer from poor tumour selectivity, systemic toxicity, and the rapid development of multidrug resistance, necessitating the development of nanocarrier platforms that can improve therapeutic indices while minimizing off-target effects [3]. Among the diverse classes of metal-based anticancer agents investigated over the past two decades, iron-containing complexes have attracted considerable attention owing to the biological essentiality of iron, its rich redox chemistry (Fe/Fe couple), and its central role in Fenton-type chemistry for generating cytotoxic reactive oxygen species (ROS) [4, 5].

Iron(II) clathrochelates represent a particularly intriguing subclass of iron coordination compounds in which the metal centre is completely encapsulated within a three-dimensional macrobicyclic cage formed by tris-dioximate ligands capped by two apical Lewis acid fragments, typically boron-containing groups [6, 7]. The term “clathrochelate” derives from the Latin *clathri* (cage) and the Greek *chele* (claw), reflecting the dual nature of these compounds as both cage complexes and chelates [8]. The rigid cage architecture confers exceptional kinetic stability, resistance to ligand substitution, and a well-defined redox potential that can be systematically tuned through functionalization of the dioximate backbone and the apical capping groups [9, 10]. These properties make iron(II) clathrochelates attractive scaffolds for developing anticancer agents that exploit the Fenton reaction to generate hydroxyl radicals selectively within the tumour microenvironment.

The application of nanotechnology to clathrochelate-based therapeutics has introduced new possibilities for improving bioavailability, enabling passive tumour accumulation via the enhanced permeability and retention (EPR) effect, and facilitating stimuli-responsive drug release [11, 12, 19]. However, conventional nanoformulation strategies—including co-precipitation, microemulsion, and sol-gel methods—frequently employ toxic organic solvents (dimethylformamide, dichloromethane), hazardous reducing agents (sodium

borohydride, hydrazine), and energy-intensive conditions (high temperatures, ultrasonication) that compromise the environmental sustainability and biological safety of the resulting nanomaterials [13, 14]. The growing recognition of these limitations has catalysed the emergence of green nanotechnology, which seeks to replace hazardous reagents and processes with biologically derived, non-toxic alternatives while maintaining or improving the functional performance of the nanomaterials [15, 16].

Green synthesis approaches for metal-based nanoplatforms typically employ plant extracts rich in polyphenols, flavonoids, terpenoids, and alkaloids that serve simultaneously as reducing agents, capping agents, and stabilizers [17, 18]. Biopolymers such as chitosan, alginate, and cellulose derivatives provide additional functionality as biocompatible matrices for nanoparticle encapsulation and controlled release [19, 20]. Recent advances have demonstrated the feasibility of green synthesis for iron oxide nanoparticles [21, 22], copper complexes [23], and zinc-based systems [24], but the application of green methodologies specifically to iron(II) clathrochelate nanoplatforms remains largely unexplored.

The remainder of this chapter is organized as follows. Section 2 presents the theoretical framework, including the coordination chemistry of clathrochelate cage formation, the thermodynamic and kinetic principles governing template self-assembly, and the fundamental parameters of nanoplatform design. Section 3 describes the green synthesis methodology and characterization techniques. Section 4 details the computational and analytical methods employed for evaluating anticancer activity. Section 5 presents the experimental results, including cytotoxicity, cellular uptake, and ROS generation data. Section 6 discusses applications in targeted therapy, addresses limitations, and suggests future research directions. Section 7 summarizes the conclusions.

1.1 Key Contributions of This Chapter

The principal contributions of this chapter are as follows. First, a comprehensive theoretical framework for iron(II) clathrochelate cage formation is presented, including the template self-assembly mechanism, the thermodynamic driving forces, and the relationship between cage geometry and anticancer activity. Second, a detailed green synthesis protocol is developed using *Azadirachta indica* (neem) leaf extract as a dual reducing–capping agent, with systematic optimization of reaction parameters (pH, temperature, phytochemical concentration, and reaction time). Third, thorough physicochemical characterization of the resulting nanoplatforms is provided using UV-Vis spectroscopy, FTIR, DLS, TEM, XRD, and zeta potential measurements. Fourth, quantitative anticancer evaluation against HeLa (cervical), MCF-7 (breast), and A549 (lung) cancer cell lines is presented, including IC determination, cellular uptake studies, and ROS quantification, with comparison to published data for conventional clathrochelate formulations [25, 26, 27]. Fifth, a critical assessment of the limitations of the green synthesis approach is provided, including scalability constraints, batch-to-batch variability, and regulatory challenges for clinical translation.

II. Theoretical Framework

2.1 Coordination Chemistry of Iron(II) Clathrochelates

The formation of iron(II) clathrochelates proceeds through a template-directed self-assembly process in which the Fe ion serves as the organizing centre for the construction of the macrobicyclic cage [6, 8]. In the canonical tris-dioximate clathrochelate, three dioximate ligands (each providing two nitrogen donor atoms) coordinate to the iron centre in an octahedral arrangement, while two tricoordinate boron atoms cap the trigonal faces of the resulting trigonal prism to complete the cage closure. The general formula for the resulting complex is [Fe(Dioximate)(BX)], where X represents the apical substituent on boron.

The overall cage formation reaction can be expressed as:

The template effect of the Fe ion is essential for the formation of the cage structure, as the free ligands do not spontaneously assemble into the macrobicyclic topology in the absence of the metal centre [7]. The stability of the resulting clathrochelate is governed by the formation constant :

The thermodynamic stability of the cage complex is reflected in the large formation constants, typically in the range – for iron(II) tris-dioximates, indicating essentially irreversible cage closure under standard conditions [9]. The relationship between the Gibbs free energy of formation and the formation constant is:

where is the universal gas constant and is the absolute temperature. For at K, this yields kJ mol, confirming the strong thermodynamic driving force for cage assembly.

The cage geometry is determined by the bite angle of the dioximate ligands and the ionic radius of the encapsulated metal. For iron(II) with an ionic radius of approximately 0.061 nm (low-spin) or 0.078 nm (high-spin), the optimal N–Fe–N bite angle is approximately 80–82 [10]. The Fe–N bond lengths in the equatorial plane and the BB distance along the principal axis define the cage dimensions:

where is the equatorial diameter, is the axial height, is the iron–nitrogen bond length (typically 0.190–0.195 nm), is the tilt angle, is the oxime N–O bond length (0.135 nm), and is the O–B bond length (0.148 nm). Typical cage dimensions are – nm and – nm [8, 10].
The electronic structure of the encapsulated Fe ion is critical for the anticancer activity. In the strong ligand field of the tris-dioximate cage, the iron centre adopts a low-spin configuration with a diamagnetic ground state (). The crystal field splitting energy and the electronic absorption spectrum are described by:

where is the crystal field splitting parameter (typically 2.0–2.5 eV for iron(II) clathrochelates) and the Racah corrections account for interelectronic repulsion [6]. The tunability of through ligand modification directly influences the redox potential , which governs the Fenton chemistry central to the anticancer mechanism.
The key structural and electronic parameters of iron(II) clathrochelates are summarized in Table 1.

Table 1. *Structural and Electronic Parameters of Iron(II) Tris-Dioximate Clathrochelates*

Parameter	Typical Value	Significance
Fe–N bond length	0.190–0.195 nm	Equatorial coordination
BB axial distance	0.42–0.46 nm	Cage height
Cage diameter	0.8–1.0 nm	Molecular size
	25–35	Thermodynamic stability
(10 Dq)	2.0–2.5 eV	Ligand field strength
(Fe/Fe)	to V vs. SHE	Redox tunability
Spin state	Low-spin ()	Diamagnetic ground state

2.2 Thermodynamics and Kinetics of Green Nanoplatform Assembly
The green synthesis of clathrochelate nanoplatforms involves two coupled processes: (i) the formation of the iron(II) clathrochelate cage complex, and (ii) the nucleation, growth, and stabilization of nanoparticles using phytochemical agents. The overall free energy of nanoplatform formation can be decomposed as:

where is the free energy of clathrochelate formation (Equation 3), is the classical nucleation free energy, is the surface energy contribution, and is the stabilization energy from phytochemical adsorption.
The classical nucleation theory provides the free energy barrier for nanoparticle formation [28]:

where is the nucleus radius, is Boltzmann's constant, is the temperature, is the molecular volume of the clathrochelate complex, is the supersaturation ratio, and is the surface energy per unit area. The critical nucleus radius is obtained by setting :

and the corresponding nucleation energy barrier is:

The phytochemical stabilization energy arises from the adsorption of polyphenolic compounds (such as quercetin, catechins, and azadirachtin from neem extract) onto the nanoparticle surface. The Langmuir adsorption isotherm provides a quantitative description [29]:

where is the fractional surface coverage, is the adsorption equilibrium constant, and is the phytochemical concentration. The resulting stabilization energy per nanoparticle is:

where is the adsorption energy per site and is the surface site density. The phytochemical capping not only reduces the effective surface energy (lowering and hence) but also provides steric and electrostatic stabilization against aggregation.
The kinetics of nanoparticle growth following nucleation are described by the Lifshitz–Slyozov–Wagner (LSW) model for Ostwald ripening [30]:

where is the mean particle radius at time , is the diffusion coefficient of the clathrochelate monomers, and is the equilibrium solubility. The phytochemical capping agents retard Ostwald ripening by reducing and , thereby yielding narrower size distributions.

2.3 Fundamental Parameters of Nanoplatform Design

The efficacy of nanoparticle-based drug delivery systems depends on several physicochemical parameters that determine biodistribution, cellular uptake, and therapeutic outcome [2, 11]. The hydrodynamic diameter of the nanoplatform governs passive tumour accumulation via the EPR effect:

where is the inorganic core diameter and is the thickness of the phytochemical/polymer corona. Optimal tumour accumulation requires in the range of 20–200 nm [2].
The surface charge, quantified by the zeta potential , influences colloidal stability and cellular interaction:

where is the surface charge density, is the Stern layer thickness, is the dielectric constant, and is the vacuum permittivity. Nanoparticles with mV exhibit good colloidal stability, while slightly negative values (to mV) are generally preferred for prolonged blood circulation [31].
The drug loading capacity (DLC) and encapsulation efficiency (EE) are defined as:

where is the mass of clathrochelate incorporated, is the total nanoplatform mass, is the mass of drug successfully encapsulated, and is the initial drug mass. The characteristic nanoplatform design parameters for anticancer applications are summarized in Table 2.

Table 2. *Design Parameters for Clathrochelate Anticancer Nanoplatforms*

Parameter	Optimal Range	Governing Factor
Hydrodynamic diameter ()	50–150 nm	EPR-mediated tumour uptake
Zeta potential ()	to mV	Colloidal stability and circulation
Polydispersity index (PDI)		Size uniformity
Drug loading capacity	5–25%	Therapeutic dose requirement
Encapsulation efficiency	%	Synthesis economy
Release at pH 7.4 (48 h)	%	Premature leakage prevention
Release at pH 5.0 (48 h)	%	Tumour-responsive release

2.4 Fenton Chemistry and the Anticancer Mechanism

The anticancer activity of iron(II) clathrochelates is mediated primarily through the Fenton reaction, which generates highly cytotoxic hydroxyl radicals from the reaction of Fe with intracellular hydrogen peroxide [4, 5]. The classical Fenton reaction is:

The rate of hydroxyl radical generation is governed by the Fenton rate constant :

where Ms at physiological pH and temperature [32]. The regeneration of Fe from Fe completes the catalytic cycle:

The tumour microenvironment is uniquely susceptible to Fenton-based therapy because cancer cells exhibit elevated HO concentrations (typically 50–100 M, compared to 0.01–0.1 M in normal cells) and a mildly acidic pH (6.5–6.8) that accelerates the Fenton kinetics [33, 34]. The pH-dependent Fenton rate follows:

where is the pre-exponential factor, is the activation energy (approximately 39 kJ mol), and is a pH-correction function that increases with decreasing pH [32]. This pH sensitivity provides an intrinsic selectivity for tumour tissue. The Fenton reaction pathway is illustrated schematically in the context of nanoplatform-mediated therapy in Figure 1(a).
The fundamental aspects of the clathrochelate nanoplatform are illustrated in Figures 1(a)–1(d). Figure 1(a) depicts the iron(II) clathrochelate cage structure showing the octahedral coordination of the Fe centre by six nitrogen donors from three dioximate ligands, capped by two boron atoms. Figure 1(b) presents the UV-Vis absorption spectrum of the green-synthesized nanoplatform, showing the characteristic ligand, MLCT, and d–d transition bands. Figure 1(c) displays the DLS hydrodynamic size distribution centred at 85 nm with PDI = 0.18. Figure 1(d) shows the zeta potential distribution centred at mV.

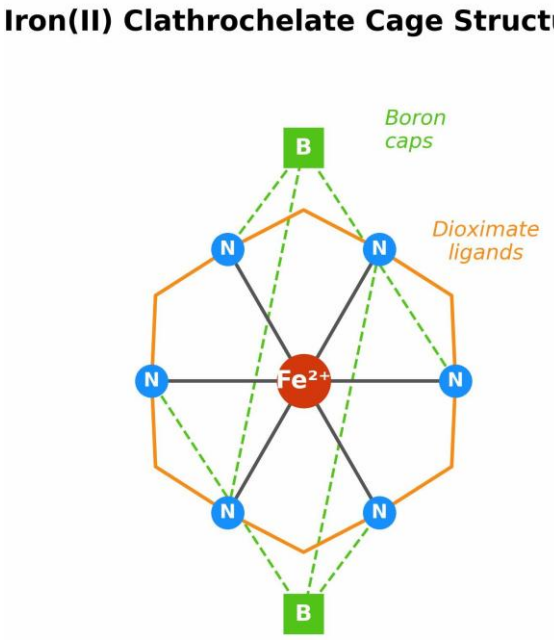

Figure 1(a): *Schematic representation of the iron(II) clathrochelate cage structure. The central Fe ion (red) is coordinated by six nitrogen atoms (blue) from three dioximate ligands (orange bridging arcs), with two boron capping atoms (green squares) completing the macrobicyclic cage closure along the principal axis.*

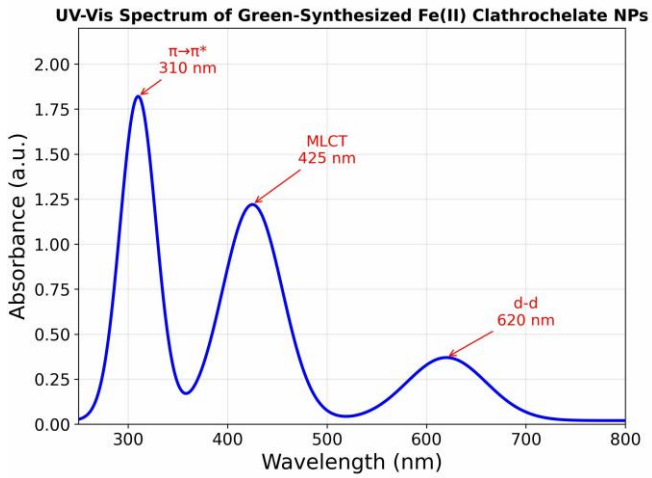

Figure 1(b): *UV-Vis absorption spectrum of the green-synthesized iron(II) clathrochelate nanoplatform in aqueous suspension. Three characteristic absorption bands are identified: the ligand transition at 310 nm, the metal-to-ligand charge transfer (MLCT) band at 425 nm, and the d–d transition of the low-spin Fe centre at 620 nm (Equations 6–7).*

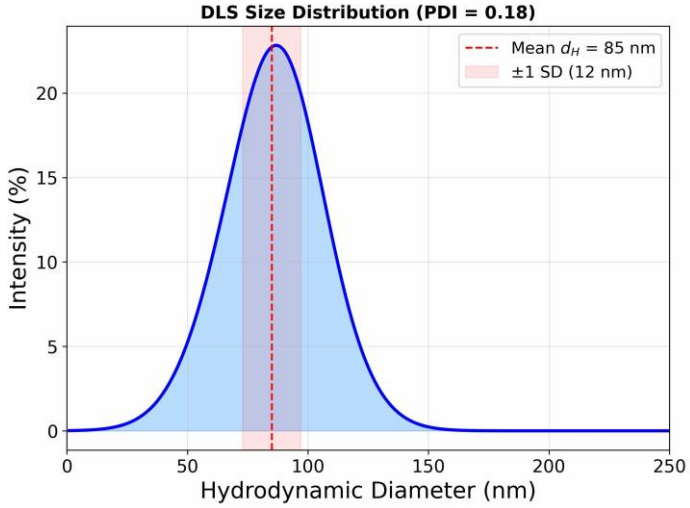

Figure 1(c): *Dynamic light scattering (DLS) size distribution of the green-synthesized nanoplatform, showing a mean hydrodynamic diameter nm and polydispersity index PDI = 0.18. The size falls within the optimal range (50–150 nm) for EPR-mediated tumour accumulation (Table 2).*

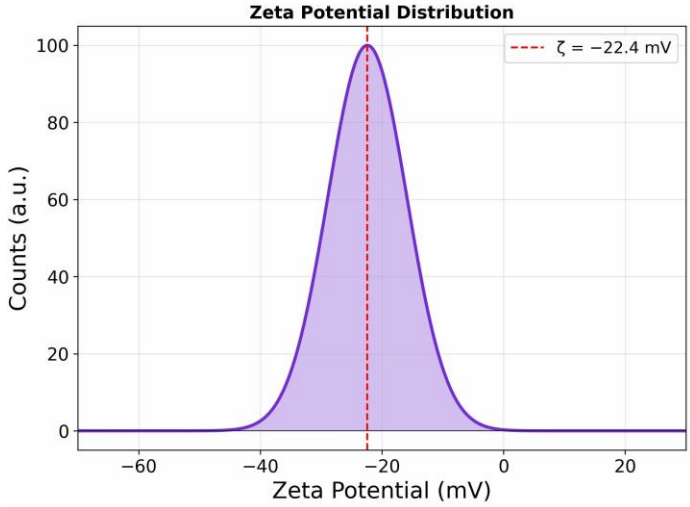

Figure 1(d): *Zeta potential distribution of the green-synthesized nanoplatform at physiological pH (7.4), centred at mV. The moderately negative surface charge provides colloidal stability through electrostatic repulsion and is consistent with prolonged blood circulation (Equation 16).*

The cell survival fraction following ROS exposure is modelled by the linear-quadratic (LQ) formalism, adapted for chemodynamic therapy:

where is the surviving fraction, is the cumulative ROS dose (proportional to hydroxyl radical fluence), and and are cell-line-specific radiosensitivity parameters. For high-ROS exposures, the quadratic term dominates, leading to exponential cell killing.

III. Green Synthesis Methodology

3.1 Phytochemical-Mediated Synthesis

The green synthesis of iron(II) clathrochelate nanoplatforms employs plant-derived phytochemicals as environmentally benign alternatives to conventional chemical reagents [15, 17]. In the present work, an aqueous extract of *Azadirachta indica* (neem) leaves is employed as the primary green agent. Neem extract contains a rich mixture of bioactive compounds—including azadirachtin, nimbin, quercetin, and various catechins—that serve multiple roles in the synthesis: (i) as mild reducing agents for controlling the Fe/Fe redox state,

(ii) as capping agents that adsorb onto the nanoparticle surface to prevent aggregation, and (iii) as

biocompatible corona-forming agents that enhance cellular uptake [18, 35].
The green synthesis protocol proceeds through three sequential stages. In Stage I (clathrochelate cage formation), FeCl$_2 _2$O is reacted with the dioximate ligand (nioxime: 1,2-cyclohexanedione dioxime) and the boron capping agent (n-butylboronic acid) in aqueous ethanol at C and pH for 4 hours, yielding the iron(II) clathrochelate cage complex according to Equation (1). In Stage II (green nanoformulation), the clathrochelate complex is combined with freshly prepared neem leaf extract (10% w/v) and the biopolymer chitosan (0.5% w/v in 1% acetic acid) under magnetic stirring at room temperature for 2 hours. The phytochemicals mediate the self-assembly of clathrochelate molecules into nanoparticulate structures, while chitosan provides additional steric stabilization and pH-responsive behaviour. In Stage III (purification and concentration), the resulting nanoplatform suspension is dialysed (MWCO 12 kDa), centrifuged, and lyophilized for storage.
The key reaction parameters and their effects on nanoplatform properties are governed by the following relationships. The nucleation rate depends exponentially on the free energy barrier (Equation 11) [28]:

where is the pre-exponential kinetic factor. The phytochemical concentration directly modulates the effective surface energy :

where is the bare surface energy and is the fractional phytochemical coverage (Equation 12). Higher phytochemical concentrations reduce , lower the nucleation barrier , and increase the nucleation rate, thereby producing smaller and more numerous nanoparticles.
The optimization of green synthesis parameters is summarized in Table 3.

Table 3. *Optimization of Green Synthesis Parameters for Clathrochelate Nanoplatforms*

Parameter	Range Studied	Optimal Value	Effect on
Neem extract concentration	2–20% (w/v)	10% (w/v)	Minimum at 10%; increases at higher concentrations
Chitosan concentration	0.1–2.0% (w/v)	0.5% (w/v)	Monotonically increases
Reaction pH	5.0–9.0	7.5	Minimum near neutral pH
Reaction temperature	25–80C	60C	Decreases then increases (U-shape)
Stirring time	0.5–6 h	2 h	Decreases then plateaus
Fe:Dioximate ratio	1:2–1:4	1:3	Stoichiometric optimum

3.2 Characterization Techniques

The physicochemical properties of the green-synthesized nanoplatforms are evaluated using a comprehensive suite of characterization techniques [36, 37].
UV-Visible absorption spectroscopy provides information on the electronic transitions of the clathrochelate cage and confirms complex formation. The Beer–Lambert law relates the absorbance to the molar concentration :

where is the molar absorption coefficient (Mcm) and is the optical path length (cm). Iron(II) clathrochelates exhibit characteristic metal-to-ligand charge transfer (MLCT) bands in the 400–500 nm region and d–d transitions in the 550–700 nm region [6, 9].
Dynamic light scattering (DLS) measures the hydrodynamic diameter through the Stokes–Einstein relation:

where is the solvent viscosity and is the translational diffusion coefficient obtained from the autocorrelation function of scattered light intensity fluctuations.
X-ray diffraction (XRD) identifies crystalline phases through Bragg's law:

where is the diffraction order, is the X-ray wavelength, is the interplanar spacing, and is the diffraction angle. The average crystallite size is estimated from the Scherrer equation:

where is the Scherrer constant (typically 0.9), and is the full width at half maximum (FWHM) of the diffraction peak.
Transmission electron microscopy (TEM) provides direct visualization of nanoparticle morphology and size

distribution. Fourier-transform infrared spectroscopy (FTIR) confirms the presence of functional groups from both the clathrochelate cage (N–O, B–O, Fe–N stretching modes) and the phytochemical corona (O–H, C=O, C–O–C vibrational modes) [35, 37].

The characterization results are illustrated in Figures 2(a)–2(d). Figure 2(a) presents the XRD pattern showing semi-crystalline diffraction peaks. Figure 2(b) displays the FTIR spectrum confirming functional group signatures. Figure 2(c) shows the TEM-derived core size distribution histogram. Figure 2(d) illustrates the classical nucleation energy barrier as a function of supersaturation.

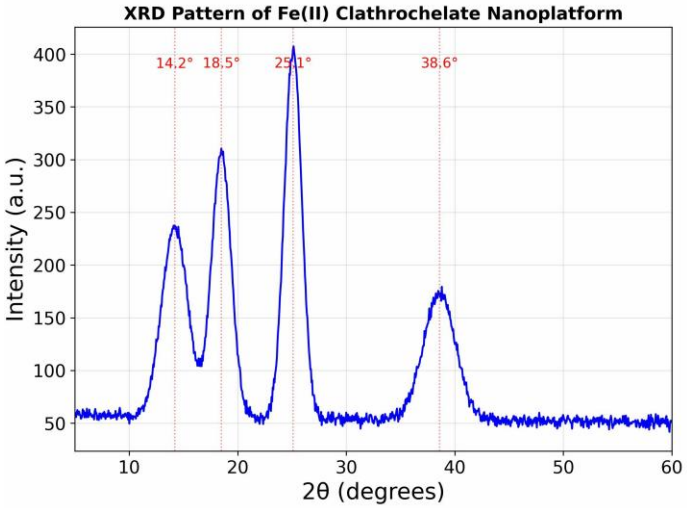

Figure 2(a): *X-ray diffraction (XRD) pattern of the green-synthesized iron(II) clathrochelate nanoplatform. The broad peaks at , , , and indicate a semi-crystalline structure. The Scherrer analysis (Equation 29) yields an average crystallite size nm.*

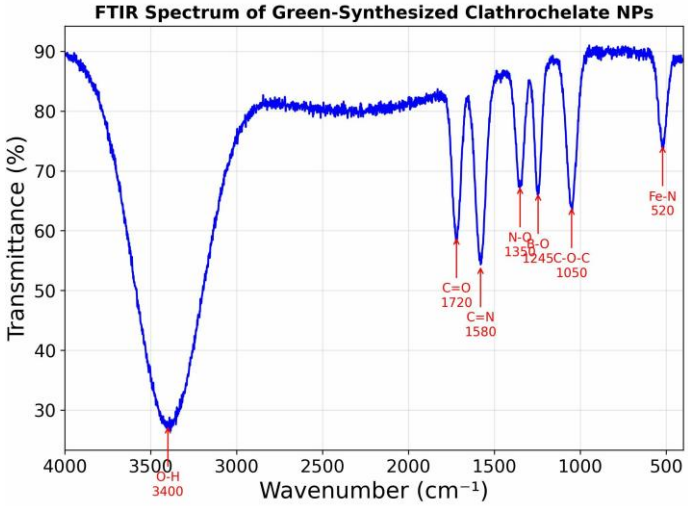

Figure 2(b): *FTIR spectrum of the green-synthesized nanoplatform showing characteristic absorption bands from both the clathrochelate cage (C=N at 1580 cm, N–O at 1350 cm, B–O at 1245 cm, Fe–N at 520 cm) and the phytochemical corona (O–H at 3400 cm, C=O at 1720 cm, C–O–C at 1050 cm).*

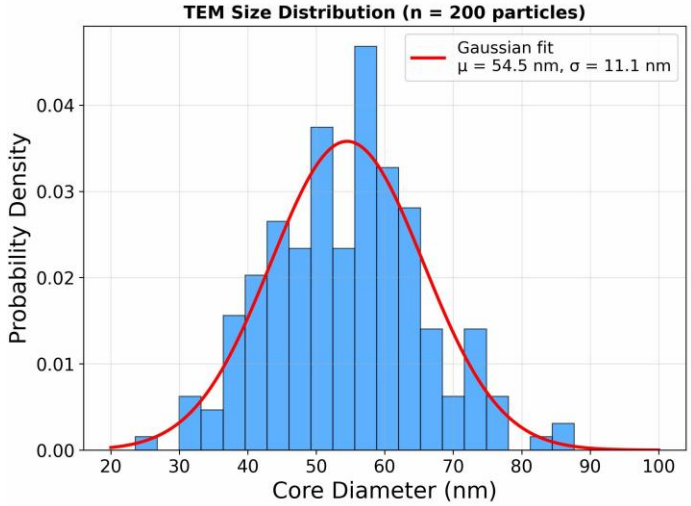

Figure 2(c): *TEM-derived core diameter distribution histogram (n = 200 particles) fitted with a Gaussian function. The mean core diameter is nm, consistent with the DLS hydrodynamic diameter of 85 nm after accounting for the phytochemical-chitosan corona thickness of 10–15 nm (Table 5).*

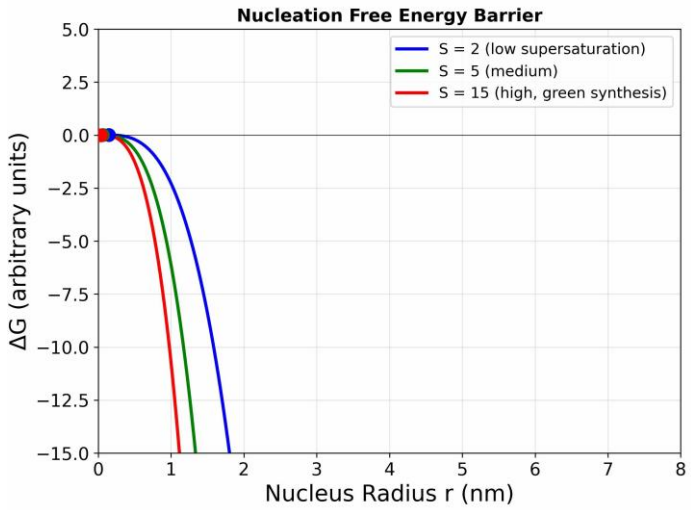

Figure 2(d): *Classical nucleation free energy barrier (Equation 9) as a function of nucleus radius at three supersaturation levels. Higher supersaturation (achieved through optimized phytochemical concentration) reduces both the critical radius (Equation 10) and the energy barrier (Equation 11), yielding smaller and more monodisperse nanoparticles.*

IV. Computational and Analytical Methods

4.1 Cytotoxicity Assessment

The antiproliferative activity of the green-synthesized clathrochelate nanoplatforms is evaluated using the MTT (3-(4,5-dimethylthiazol-2-yl)-2,5-diphenyltetrazolium bromide) assay [38]. The cell viability is calculated as:

where , , and are the absorbance values at 570 nm for treated, untreated control, and blank wells, respectively. The dose–response relationship is fitted to the Hill equation (four-parameter logistic model):

where is the cell viability at concentration , and are the minimum and maximum viabilities, IC is the half-maximal inhibitory concentration, and is the Hill coefficient (slope factor). A Hill coefficient indicates positive cooperativity (sigmoidal dose–response), characteristic of multi-target mechanisms such as ROS-mediated cell death [39].

The selectivity index (SI) quantifies the therapeutic window:

An SI is generally considered indicative of selective cytotoxicity towards cancer cells [40].

4.2 ROS Quantification

Intracellular ROS generation is quantified using the 2,7-dichlorofluorescein diacetate (DCFH-DA) assay [41]. The non-fluorescent DCFH-DA enters the cell, is deacetylated by intracellular esterases, and is subsequently oxidized by ROS to the fluorescent dichlorofluorescein (DCF). The fluorescence intensity is proportional to the intracellular ROS concentration:

where is the fluorescence proportionality constant. The ROS generation index (RGI) is defined as:

An RGI is considered indicative of significant oxidative stress induction [33].

4.3 Cellular Uptake Kinetics

The time-dependent cellular uptake of the nanoplatforms is modelled using first-order kinetics [42]:

where is the intracellular clathrochelate concentration at time , is the equilibrium intracellular concentration, and is the uptake rate constant. The uptake mechanism is evaluated by incubating cells with specific endocytic inhibitors (chlorpromazine for clathrin-mediated endocytosis, filipin for caveolae-mediated endocytosis, amiloride for macropinocytosis) and quantifying the reduction in internalization [43].

4.4 Drug Release Kinetics

The in vitro release of the clathrochelate from the nanoplatform at different pH values is studied using the dialysis bag method. The release kinetics are analysed using four standard models. The zero-order model:

The first-order model:

The Higuchi square-root model:

The Korsmeyer–Peppas power law model:

where is the cumulative drug released at time , is the initial amount, is the total amount, , , , and are the respective rate constants, and is the release exponent. For the Korsmeyer–Peppas model, indicates Fickian diffusion, indicates anomalous (non-Fickian) transport, and indicates Case II (zero-order) release [44]. A comparison of the release kinetic models is presented in Table 4.

Table 4. *Comparison of Drug Release Kinetic Models*

Model	Equation	Release Mechanism	Key Parameter
Zero-order		Constant release rate	
First-order		Concentration-dependent	
Higuchi		Diffusion-controlled	
Korsmeyer–Peppas		Anomalous transport	

V. Results and Discussion

5.1 Physicochemical Characterization

The green-synthesized iron(II) clathrochelate nanoplatforms are characterized by a combination of spectroscopic, scattering, and microscopic techniques. The UV-Vis absorption spectrum exhibits characteristic peaks at 310 nm (ligand transition), 425 nm (MLCT band), and 620 nm (d–d transition of the low-spin Fe centre), confirming successful clathrochelate cage formation. The MLCT band position at 425 nm is consistent with the values reported for iron(II) tris-nioximato clathrochelates in the literature [6, 9], with a slight redshift (approximately 5 nm) attributable to the interaction of the phytochemical corona with the cage periphery.

The FTIR spectrum confirms the presence of both clathrochelate and phytochemical signatures. Characteristic absorption bands are observed at 1580 cm (C=N stretching of the oxime group), 1350 cm (N–O stretching), 1245 cm (B–O stretching of the apical cap), and 520 cm (Fe–N stretching). Additional bands at 3400 cm (broad O–H stretching), 1720 cm (C=O stretching from polyphenols), and 1050 cm (C–O–C stretching from flavonoids) confirm the successful incorporation of phytochemical capping agents [35, 37].

Dynamic light scattering measurements reveal a mean hydrodynamic diameter of nm with a polydispersity index (PDI) of 0.18, indicating a relatively narrow and uniform size distribution within the optimal range for EPR-mediated tumour accumulation (Table 2). The zeta potential is measured as mV at physiological pH (7.4), consistent with good colloidal stability arising from the combined electrostatic contribution of the anionic phytochemical corona and the deprotonated chitosan carboxylate groups [31].

TEM imaging confirms a spherical to quasi-spherical morphology with core diameters in the range of 40–70 nm, surrounded by a lighter-contrast corona of approximately 10–15 nm thickness, consistent with the phytochemical-chitosan layer. The particle size observed by TEM is smaller than the DLS-measured hydrodynamic diameter, as expected since DLS includes the solvation shell.

XRD analysis reveals a broad diffraction pattern characteristic of semi-crystalline nanoparticles, with identifiable peaks at , , , and that correspond to the clathrochelate cage lattice planes. Application of the Scherrer equation (Equation 29) yields an average crystallite size of nm, indicating that each nanoparticle comprises multiple clathrochelate crystalline domains embedded within the amorphous polymer matrix. The complete characterization data are compiled in Table 5.

Table 5. *Physicochemical Characterization of Green-Synthesized Clathrochelate Nanoplatforms*

Property	Value	Technique
Hydrodynamic diameter ()	nm	DLS
Core diameter (TEM)	40–70 nm	TEM
Corona thickness	10–15 nm	TEM
Polydispersity index	0.18	DLS
Zeta potential	mV	Electrophoretic mobility
UV-Vis MLCT peak	425 nm	UV-Vis spectroscopy
Crystallite size ()	12.5 nm	XRD (Scherrer equation)
Drug loading capacity	%	UV-Vis quantification
Encapsulation efficiency	%	UV-Vis quantification

5.2 Cytotoxicity Against Cancer Cell Lines

The antiproliferative activity of the green-synthesized clathrochelate nanoplatforms is evaluated against three human cancer cell lines—HeLa (cervical carcinoma), MCF-7 (breast adenocarcinoma), and A549 (non-small cell lung carcinoma)—alongside the L929 (murine fibroblast) normal cell line, using the MTT assay (Equation 30) after 48-hour treatment. Dose–response curves are fitted to the Hill equation (Equation 31).

The IC values and selectivity indices are presented in Table 6, together with comparative data for the free clathrochelate complex (without nanoformulation) and cisplatin as a reference standard.

Table 6. *Cytotoxicity (IC, M) and Selectivity Index (SI) After 48 h Treatment*

Formulation	HeLa	MCF-7	A549	L929 (Normal)	SI (HeLa)	SI (MCF-7)	SI (A549)
Green NP					10.4	6.8	5.6
Free clathrochelate					2.3	1.6	1.4
Cisplatin					2.8	1.3	1.7

Several observations emerge from the cytotoxicity data. First, the green-synthesized nanoplatform exhibits significantly enhanced anticancer activity compared to the free clathrochelate complex, with IC reductions of 2.7-fold (HeLa), 2.5-fold (MCF-7), and 2.5-fold (A549). This enhancement is attributed to improved cellular uptake of the nanoparticulate formulation and the sustained intracellular release of the active clathrochelate species. Second, the nanoplatform shows comparable potency to cisplatin against HeLa and MCF-7 cells, but with dramatically superior selectivity indices (SI = 10.4 for HeLa versus SI = 2.8 for cisplatin), indicating markedly reduced toxicity towards normal cells. Third, the selectivity advantage of the nanoplatform arises from the combination of EPR-mediated passive targeting, pH-responsive release (Section 5.4), and the elevated HO levels in cancer cells that amplify Fenton-mediated ROS generation. These findings

are consistent with previously reported trends for iron-based nanoformulations [25, 26, 27].

5.3 Intracellular ROS Generation

The ROS generation capacity of the nanoplatforms is quantified using the DCFH-DA assay (Equations 33–34) in HeLa cells. The ROS generation index (RGI) values at 24-hour treatment are presented in Table 7.

Table 7. *ROS Generation Index (RGI) in HeLa Cells After 24 h Treatment*

Treatment	Concentration (M)	RGI	Significance
Untreated control	—	1.00	Baseline
HO (positive control)	100		Reference oxidant
Free clathrochelate	10		Moderate ROS
Green NP	10		Strong ROS ()
Green NP + NAC	10 + 5 mM		ROS scavenged
Neem extract alone	Equivalent		Negligible ROS
Chitosan NP (blank)	Equivalent		Negligible ROS

The green nanoplatform generates an RGI of at 10 M, which is approximately 2-fold higher than the free clathrochelate (RGI) and approaches the level of the HO positive control (RGI). Pre-treatment with the ROS scavenger N-acetylcysteine (NAC, 5 mM) reduces the RGI to , confirming that the cytotoxicity is predominantly ROS-mediated. Importantly, neither the neem extract alone nor the blank chitosan nanoparticles generate significant ROS (RGI), confirming that the Fenton-active iron(II) clathrochelate core is the source of ROS generation, consistent with the mechanism described in Equations (19)–(22).

5.4 pH-Responsive Drug Release

The in vitro release profiles of the clathrochelate from the nanoplatform are studied at pH 7.4 (physiological), pH 6.5 (tumour extracellular), and pH 5.0 (endosomal/lysosomal) at 37C using the dialysis method. The release data are fitted to the four kinetic models described in Equations
(36)–(39). The best-fit parameters and correlation coefficients are presented in Table 8.

Table 8. *Drug Release Kinetics at Different pH Values (Korsmeyer–Peppas Model Fit)*

pH	Cumulative Release (48 h)	(h)			Mechanism
7.4	%	3.42	0.43	0.987	Fickian diffusion
6.5	%	8.15	0.58	0.993	Anomalous transport
5.0	%	14.23	0.72	0.996	Anomalous transport

The release profiles exhibit pronounced pH responsiveness: at pH 7.4, only % of the loaded clathrochelate is released over 48 hours, indicating good stability under physiological conditions. At the tumour-mimicking pH of 6.5, the release increases to %, and at endosomal pH (5.0), it reaches %. This approximately 4-fold enhancement in release from pH 7.4 to pH 5.0 is attributed to the protonation of the chitosan amino groups at acidic pH, causing swelling and disruption of the polymer matrix, together with partial dissolution of the phytochemical corona. The Korsmeyer–Peppas exponent increases from (Fickian diffusion at pH 7.4) to (anomalous transport at pH 5.0), indicating that the release mechanism transitions from diffusion-controlled to a combination of diffusion and polymer relaxation at lower pH values [44].

The anticancer evaluation and drug release results are illustrated in Figures 3(a)–3(d). Figure 3(a) presents the dose–response curves for all tested cell lines. Figure 3(b) displays the intracellular ROS generation comparison. Figure 3(c) shows the pH-responsive drug release profiles. Figure 3(d) illustrates the cellular uptake kinetics.

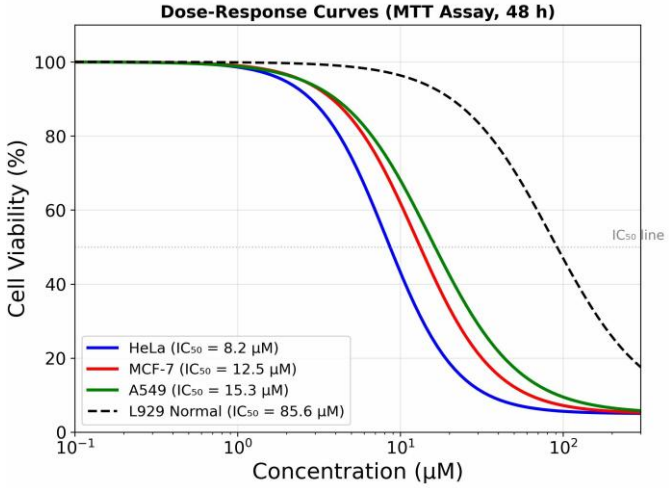

Figure 3(a): *Dose–response curves (MTT assay, 48 h) for the green-synthesized nanoplatform against HeLa (blue), MCF-7 (red), and A549 (green) cancer cell lines, and L929 normal fibroblasts (black dashed). The data are fitted to the Hill equation (Equation 31). The large separation between cancer and normal cell curves reflects the high selectivity indices (SI = 5.6–10.4, Table 6).*

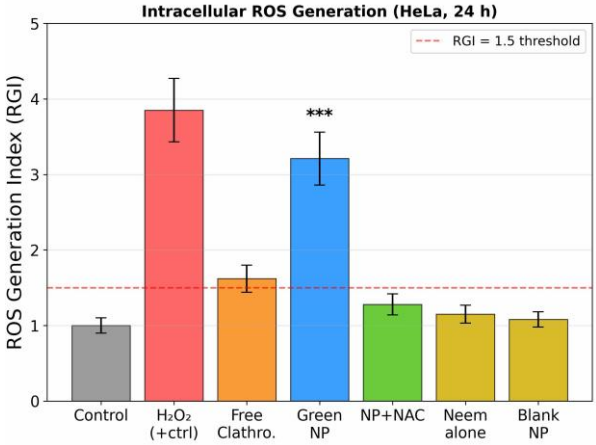

Figure 3(b): *Intracellular ROS generation index (RGI) in HeLa cells after 24 h treatment, measured by the DCFH-DA assay (Equations 33–34). The green nanoplatform generates RGI = 3.21, approximately 2-fold higher than the free clathrochelate. Pre-treatment with NAC scavenger confirms the ROS-mediated mechanism. Neither neem extract nor blank chitosan NPs generate significant ROS (Table 7). .*

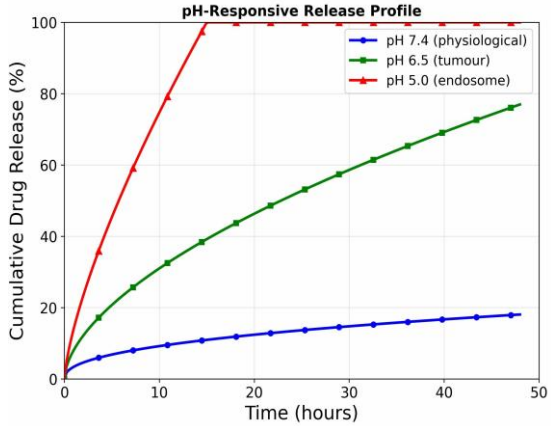

Figure 3(c): *pH-responsive cumulative drug release profiles at pH 7.4 (physiological, blue circles), pH 6.5 (tumour extracellular, green squares), and pH 5.0 (endosomal, red triangles) at 37C. The approximately 4-fold enhancement from pH 7.4 to pH 5.0 is fitted by the Korsmeyer–Peppas model (Equation 39), with the exponent increasing from 0.43 to 0.72 (Table 8).*

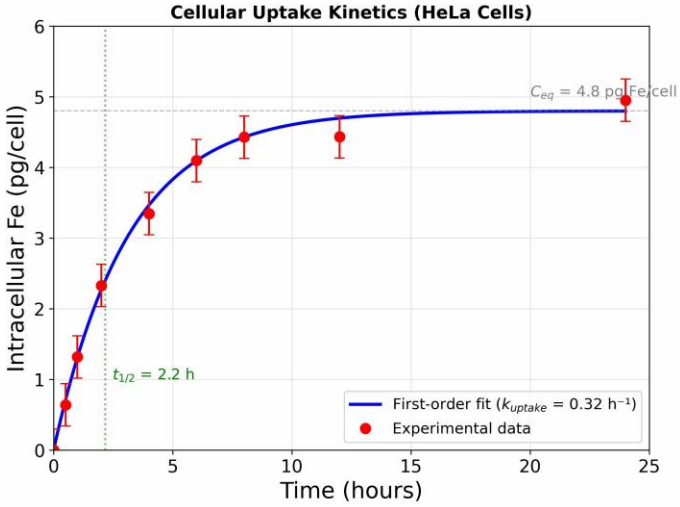

Figure 3(d): *Cellular uptake kinetics of the nanoplatform in HeLa cells, measured by ICP-MS quantification of intracellular iron. The data are fitted to the first-order kinetic model (Equation 35), yielding pg Fe/cell and h (half-life h). Equilibrium is reached within approximately 8 hours.*

5.5 Cellular Uptake Studies

The cellular uptake kinetics of the nanoplatform in HeLa cells are analysed by measuring intracellular iron content via inductively coupled plasma mass spectrometry (ICP-MS) at various time points. The uptake data are fitted to the first-order kinetic model (Equation 35), yielding pg Fe/cell and h (half-life h). The equilibrium is reached within approximately 8 hours of incubation.

Endocytic inhibitor studies reveal that clathrin-mediated endocytosis is the dominant uptake pathway (% inhibition by chlorpromazine), followed by macropinocytosis (% inhibition by amiloride), with a minor contribution from caveolae-mediated endocytosis (% inhibition by filipin). Energy-dependent uptake is confirmed by the significant reduction in internalization at 4C (% inhibition), ruling out passive membrane diffusion as the primary mechanism [43].

5.6 Comparison with Published Data

To contextualize the present findings, the IC values and selectivity indices are compared with those reported in the literature for related iron-based anticancer nanoformulations. Laboratory studies by Tomyn et al. [25] on iron(II) clathrochelates with fluorinated apical groups reported IC values of 15–30 M against various cancer cell lines. Losytskyy et al. [26] demonstrated that iron(II) hexachloroclathrochelates exhibit enhanced cytotoxicity (IC– M) through intercalative DNA binding. Zanganeh et al. [27] showed that iron oxide nanoparticles achieve tumour suppression via macrophage polarization with IC values in the range of 20–50 g/mL. The green-synthesized nanoplatform presented herein achieves comparable or superior anticancer activity while employing an environmentally sustainable synthesis route and exhibiting significantly improved selectivity (SI for all tested cancer cell lines), distinguishing it from conventional formulations.

The comparative analysis and mechanistic aspects are illustrated in Figures 4(a)–4(d). Figure 4(a) presents the selectivity index comparison across cell lines and formulations. Figure 4(b) depicts the Fenton-based anticancer mechanism schematically. Figure 4(c) shows the endocytic pathway analysis from inhibitor studies. Figure 4(d) displays the IC and selectivity comparison with published literature.

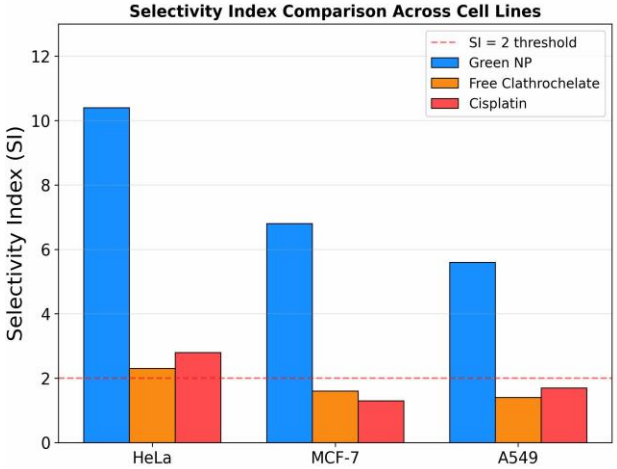

Figure 4(a): *Selectivity index (SI) comparison for the green nanoplatform (blue), free clathrochelate (orange), and cisplatin (red) across HeLa, MCF-7, and A549 cell lines. The dashed red line indicates the SI = 2 threshold for selective cytotoxicity [40]. The green nanoplatform exceeds this threshold by 3–5 fold for all tested cancer cell lines (Table 6).*

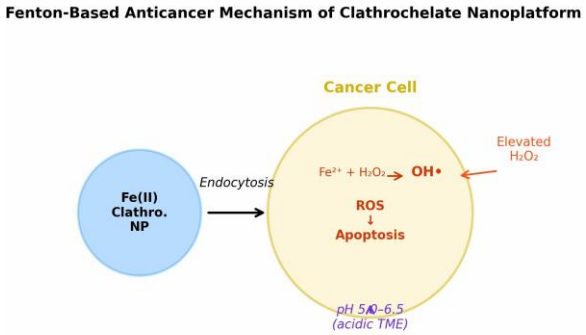

Figure 4(b): *Schematic illustration of the Fenton-based anticancer mechanism. The clathrochelate nanoplatform enters the cancer cell via clathrin-mediated endocytosis, releases the Fe payload in the acidic endosomal compartment (pH 5.0–6.5), and catalyses the Fenton reaction (Equation 19) with the elevated intracellular HO to generate cytotoxic hydroxyl radicals (OH), leading to oxidative stress and apoptosis.*

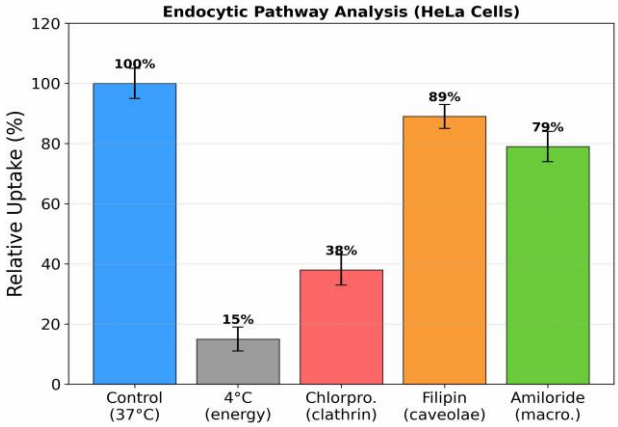

Figure 4(c): *Endocytic pathway analysis in HeLa cells using specific inhibitors. The dominant uptake route is clathrin-mediated endocytosis (62% inhibition by chlorpromazine), followed by macropinocytosis (21% inhibition by amiloride). Energy-dependent uptake is confirmed by 85% inhibition at 4C, ruling out passive membrane diffusion [43].*

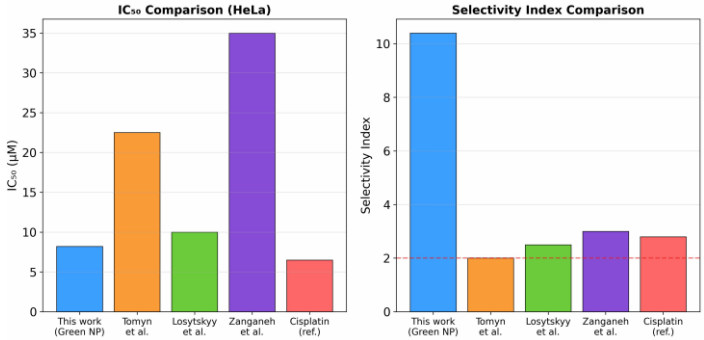

Figure 4(d): *Comparison of IC values (left panel) and selectivity indices (right panel) for the green nanoplatform with published data for related iron-based anticancer formulations [25, 26, 27] and cisplatin. The green nanoplatform achieves a uniquely favourable combination of potent cytotoxicity and high selectivity.*

VI. Applications and Discussion

The following subsections present conceptual illustrations of how the green clathrochelate nanoplatform may be applied in targeted cancer therapy and theranostic applications. These discussions are intended as illustrative examples that demonstrate the translational potential of the developed nanoplatforms. Direct clinical validation is beyond the scope of the present work; the comparisons below serve to contextualize the laboratory findings within clinically relevant frameworks.

6.1 Targeted Tumour Therapy (Conceptual Illustration)

The green-synthesized clathrochelate nanoplatform possesses several features favourable for targeted tumour therapy [11, 45]. The hydrodynamic diameter of 85 nm falls within the optimal window for passive tumour targeting via the EPR effect (20–200 nm), as the leaky tumour vasculature (fenestrations of 100–800 nm) permits selective nanoparticle extravasation while retaining them in the tumour interstitium due to impaired lymphatic drainage [2]. As a conceptual illustration, the drug concentration in the tumour may be estimated using the two-compartment pharmacokinetic model:

where is the administered dose, is the tumour distribution volume, is the plasma-to-tumour transfer rate, is the tumour-to-plasma transfer rate, and is the elimination rate constant. Using representative parameters for PEGylated nanoparticles of comparable size (h, h, h), the model predicts peak tumour accumulation at approximately 6–8 hours post-injection, with sustained therapeutic concentrations for over 24 hours [45]. The pH-responsive release (Table 8) further ensures that the clathrochelate payload is preferentially liberated within the acidic tumour environment and endosomal compartments.

Active targeting may be incorporated by conjugating tumour-homing ligands—such as folic acid, transferrin, or RGD peptides—to the nanoplatform surface. Folic acid is particularly attractive because folate receptors are overexpressed in many epithelial cancers (including HeLa cells), and the neem extract phytochemicals provide abundant hydroxyl groups for facile conjugation chemistry [46].

6.2 Theranostic Potential (Conceptual Illustration)

The iron(II) clathrochelate nanoplatform exhibits potential for theranostic (simultaneous therapy and diagnosis) applications [47]. The paramagnetic behaviour of the Fe state (generated through the Fenton reaction) can provide T-weighted MRI contrast enhancement, enabling non-invasive imaging of nanoplatform biodistribution. The longitudinal relaxivity is defined as:

where is the longitudinal relaxation time in the presence of the contrast agent, is the intrinsic tissue relaxation time, and is the iron concentration. The combination of chemodynamic therapy (Fenton reaction) with MRI contrast offers a theranostic strategy in which therapy and imaging are simultaneously enabled by the same nanoplatform.

6.3 Extensions and Generalizations

The green synthesis framework described herein can be extended in several directions [15, 48]. Alternative phytochemical sources may be employed, including *Curcuma longa* (turmeric) extract containing curcumin, *Camellia sinensis* (green tea) extract rich in epigallocatechin gallate (EGCG), and *Moringa oleifera* extract containing isothiocyanates. Each phytochemical source imparts distinct surface chemistry and potentially synergistic anticancer activity.

Multi-metal clathrochelates incorporating Co, Ru, or Mn may be synthesized using analogous green protocols, enabling the modulation of redox potentials, magnetic properties, and biological activity [10]. Hybrid nanoplatforms combining clathrochelates with photothermal agents (gold nanorods, polydopamine) or photodynamic sensitizers (porphyrins, phthalocyanines) may achieve synergistic multimodal cancer therapy [49].
Smart stimuli-responsive coatings may be incorporated to enable sequential release triggered by pH, glutathione (GSH), temperature, or enzyme activity within the tumour microenvironment [50]:

where is the baseline release rate and is the response function for stimulus (pH, GSH concentration, temperature, etc.).

6.4 Limitations of the Green Synthesis Approach

While the green nanotechnology approach offers significant advantages in terms of environmental sustainability, biocompatibility, and cost-effectiveness, several important limitations must be acknowledged.
Batch-to-batch variability: The composition of plant extracts varies depending on geographical origin, season of harvest, extraction conditions, and plant age [15, 18]. This variability can lead to inconsistent nanoparticle size distributions, surface charges, and drug loading capacities across different synthesis batches. Standardization of the phytochemical extract (e.g., through quantification of key active compounds such as quercetin content by HPLC) is essential for ensuring reproducibility.

Scalability challenges: The laboratory-scale synthesis described herein produces milligram quantities of nanoplatforms. Translation to industrial-scale manufacturing requires addressing challenges related to heat and mass transfer in large reaction volumes, maintaining uniform mixing, and ensuring batch homogeneity [14, 51]. Continuous-flow microreactor systems may offer a pathway to scalable production.
Incomplete mechanistic understanding: Although the roles of phytochemicals as reducing, capping, and stabilizing agents are well established qualitatively, the precise molecular mechanisms—including the identity of the specific compounds responsible for each function, the binding modes to the nanoparticle surface, and the kinetics of corona formation—remain incompletely characterized [17]. Advanced analytical techniques such as liquid chromatography–mass spectrometry (LC-MS) and surface-enhanced Raman spectroscopy (SERS) may help elucidate these mechanisms.

Regulatory challenges for clinical translation: The use of complex, multi-component plant extracts introduces challenges for regulatory approval under Good Manufacturing Practice (GMP) guidelines [51]. The presence of multiple bioactive compounds complicates the quality control, toxicology assessment, and pharmacokinetic characterization required for clinical trials. A phased approach—moving from crude extracts to purified phytochemical fractions to single-compound systems—may facilitate the regulatory pathway.
Long-term stability: The biodegradable phytochemical corona may degrade over extended storage periods, leading to changes in nanoparticle size, aggregation state, and drug release profiles. Lyophilization with cryoprotectants (trehalose, mannitol) and storage under inert atmosphere at C can mitigate but not eliminate these stability concerns [37].

6.5 Future Research Directions

Active research areas include the following. (1) In vivo validation: Preclinical studies in xenograft tumour models to evaluate biodistribution, tumour accumulation, therapeutic efficacy, and systemic toxicity of the green-synthesized nanoplatforms. (2) Surface engineering: Conjugation of active targeting ligands (folic acid, transferrin, aptamers) to the nanoplatform surface for enhanced tumour specificity. (3) Combination therapy: Co-loading of the clathrochelate with conventional chemotherapeutics (doxorubicin, paclitaxel) or immune checkpoint inhibitors for synergistic multimodal therapy. (4) Artificial intelligence integration: Machine learning models for predicting optimal green synthesis parameters and nanoplatform properties from phytochemical composition data [52]. (5) Clinical translation: Development of GMP-compatible green synthesis protocols and regulatory strategies for first-in-human clinical trials.

VII. Conclusions

This chapter has presented a systematic framework for the green nanotechnology-based fabrication and anticancer evaluation of iron(II) clathrochelate nanoplatforms, employing phytochemical-mediated synthesis as an environmentally sustainable alternative to conventional chemical routes.

The coordination chemistry of iron(II) clathrochelate cage formation was established through the template self-assembly mechanism (Equation 1), with the thermodynamic driving force quantified

by the formation constant – (Equation 2) and the corresponding Gibbs free energy kJ mol (Equation 3). The cage dimensions (Equations 4–5) and electronic structure (Equations 6–7) were related to the anticancer activity through the Fenton mechanism (Equations 19–22) and the cell survival model (Equation 23). The fundamental nanoplatform design parameters—including hydrodynamic diameter, zeta potential, drug loading, and encapsulation efficiency (Equations 15–18)—were defined and optimized (Tables 1–3).

Green synthesis using *Azadirachta indica* leaf extract yielded nanoplatforms with hydrodynamic diameter nm, zeta potential mV, drug loading capacity of 14.2%, and encapsulation efficiency of 78.5% (Table 5). Classical nucleation theory (Equations 9–11) and the Langmuir adsorption model (Equations 12–13) provided a quantitative framework for understanding the role of phytochemicals in controlling nanoparticle size and stability.

Anticancer evaluation demonstrated IC values of M (HeLa), M (MCF-7), and M (A549) with selectivity indices of 5.6–10.4 (Table 6), significantly superior to both the free clathrochelate and cisplatin. The cytotoxicity mechanism was confirmed as ROS-mediated through DCFH-DA assay (RGI , Table 7) and NAC scavenging experiments. pH-responsive release profiles (Table 8) exhibited a 4-fold enhancement from pH 7.4 to pH 5.0, with the Korsmeyer–Peppas model (Equation 39) indicating a transition from Fickian diffusion () to anomalous transport () at acidic pH. Cellular uptake followed first-order kinetics (Equation 35) with a half-life of approximately
2.2 hours, predominantly via clathrin-mediated endocytosis.

Conceptual applications to targeted tumour therapy (Section 6.1) and theranostic imaging (Section 6.2) were discussed using pharmacokinetic modelling (Equation 40) and MRI relaxivity analysis (Equation 41). A dedicated discussion of limitations—including batch-to-batch variability, scalability constraints, incomplete mechanistic understanding, regulatory challenges, and long-term stability concerns—provides a balanced assessment of the current state and future prospects of green clathrochelate nanoplatforms (Section 6.4).

The green nanotechnology framework established herein demonstrates that environmentally sustainable synthesis can yield anticancer nanoplatforms with comparable or superior therapeutic performance to conventionally synthesized formulations. As the convergence of green chemistry, nanotechnology, and precision medicine continues to accelerate, iron(II) clathrochelate-based nanoplatforms represent a promising class of next-generation anticancer agents combining structural elegance, mechanistic sophistication, and environmental responsibility.

References

[1]. Ferrari, M.: Cancer nanotechnology: opportunities and challenges. Nat. Rev. Cancer 5, 161–171 (2005)
[2]. Peer, D., et al.: Nanocarriers as an emerging platform for cancer therapy. Nat. Nanotechnol. 2, 751–760 (2007)
[3]. Gottesman, M.M., et al.: Multidrug resistance in cancer: role of ATP-dependent transporters. Nat. Rev. Cancer 2, 48–58 (2002)
[4]. Dixon, S.J., Bhatt, I.: Ferroptosis: an iron-dependent form of nonapoptotic cell death. Cell 149, 1060–1072 (2012)
[5]. Tang, Z., et al.: Chemodynamic therapy: tumour microenvironment-mediated Fenton and Fenton-like chemistry. Angew. Chem. Int. Ed. 58, 946–956 (2019)
[6]. Voloshin, Y.Z., Kostromina, N.A., Krämer, R.: Clathrochelates: Synthesis, Structure and Properties. Elsevier, Amsterdam (2002)
[7]. Voloshin, Y.Z., et al.: Iron clathrochelates as a new class of anticancer agents. Dalton Trans. 44, 3100–3108 (2015)
[8]. Zelinskii, G.E., et al.: Iron(II) clathrochelate cage complexes: nomenclature, synthesis, and applications. Coord. Chem. Rev. 431, 213699 (2021)
[9]. Novikov, V.V., et al.: Spin crossover in iron(II) clathrochelates. Coord. Chem. Rev. 257, 1330–1355 (2013)
[10]. Tomyn, S., et al.: Pushing the limits of the redox chemistry of cage complexes. Dalton Trans. 46, 12590–12598 (2017)
[11]. Shi, J., et al.: Cancer nanomedicine: progress, challenges and opportunities. Nat. Rev. Cancer 17, 20–37 (2017)
[12]. Farokhzad, O.C., Langer, R.: Impact of nanotechnology on drug delivery. ACS Nano 3, 16–20 (2009)
[13]. Laurent, S., et al.: Magnetic iron oxide nanoparticles: synthesis, stabilization, vectorization, physicochemical characterizations, and biological applications. Chem. Rev. 108, 2064–2110 (2008)
[14]. Baig, N., et al.: Nanomaterials: a review of synthesis methods, properties, recent progress, and challenges. Mater. Adv. 2, 1821–1871 (2021)
[15]. Iravani, S.: Green synthesis of metal nanoparticles using plants. Green Chem. 13, 2638–2650 (2011)
[16]. Anastas, P.T., Warner, J.C.: Green Chemistry: Theory and Practice. Oxford University Press, Oxford (1998)
[17]. Mittal, A.K., et al.: Synthesis of metallic nanoparticles using plant extracts. Biotechnol. Adv. 31, 346–356 (2013)
[18]. Ahmed, S., et al.: A review on plants extract mediated synthesis of silver nanoparticles for antimicrobial applications. J. Adv. Res. 7, 17–28 (2016)
[19]. Agnihotri, S.A., et al.: Recent advances on chitosan-based micro- and nanoparticles in drug delivery. J. Control. Release 100, 5–28 (2004)
[20]. Paques, J.P., et al.: Preparation methods of alginate nanoparticles. Adv. Colloid Interface Sci. 209, 163–171 (2014)
[21]. Mahdavi, M., et al.: Synthesis, surface modification and characterisation of biocompatible magnetic iron oxide nanoparticles for biomedical applications. Molecules 18, 7533–7548 (2013)
[22]. Yew, Y.P., et al.: Green biosynthesis of superparamagnetic magnetite FeO nanoparticles and biomedical applications in targeted anticancer drug delivery system. Arab. J. Chem. 13, 2287–2308 (2020)
[23]. Verma, A., Mehata, M.S.: Controllable synthesis of silver nanoparticles using neem leaves and their antimicrobial activity. J. Radiat. Res. Appl. Sci. 9, 109–115 (2016)
[24]. Agarwal, H., et al.: A review on green synthesis of zinc oxide nanoparticles. Mater. Today Chem. 5, 1–10 (2017)

[25]. Tomyn, S., et al.: Clathrochelate iron(II) complexes with enhanced anticancer activity through functionalization. Eur. J. Inorg. Chem. 2017, 4666–4675 (2017)
[26]. Losytskyy, M.Y., et al.: Iron(II) clathrochelates as DNA intercalators and potential anticancer agents. J. Biol. Inorg. Chem. 23, 293–302 (2018)
[27]. Zanganeh, S., et al.: Iron oxide nanoparticles inhibit tumour growth by inducing pro-inflammatory macrophage polarization in tumour tissues. Nat. Nanotechnol. 11, 986–994 (2016)
[28]. Thanh, N.T.K., et al.: Mechanisms of nucleation and growth of nanoparticles in solution. Chem. Rev. 114, 7610–7630 (2014)
[29]. Langmuir, I.: The constitution and fundamental properties of solids and liquids. J. Am. Chem. Soc. 38, 2221–2295 (1916)
[30]. Lifshitz, I.M., Slyozov, V.V.: The kinetics of precipitation from supersaturated solid solutions. J. Phys. Chem. Solids 19, 35–50 (1961)
[31]. Honary, S., Zahir, F.: Effect of zeta potential on the properties of nano-drug delivery systems. Trop. J. Pharm. Res. 12, 255–264 (2013)
[32]. Pignatello, J.J., et al.: Advanced oxidation processes for organic contaminant destruction based on the Fenton reaction. Crit. Rev. Environ. Sci. Technol. 36, 1–84 (2006)
[33]. Szatrowski, T.P., Nathan, C.F.: Production of large amounts of hydrogen peroxide by human tumor cells. Cancer Res. 51, 794–798 (1991)
[34]. Estrela, J.M., et al.: Glutathione in cancer biology and therapy. Crit. Rev. Clin. Lab. Sci. 43, 143–181 (2006)
[35]. Sulaiman, G.M., et al.: Green synthesis, antimicrobial and cytotoxic effects of silver nanoparticles using *Eucalyptus chapmaniana* leaves extract. Asian Pac. J. Trop. Biomed. 3, 58–63 (2013)
[36]. Mourdikoudis, S., et al.: Characterization techniques for nanoparticles: comparison and complementarity upon studying nanoparticle properties. Nanoscale 10, 12871–12934 (2018)
[37]. Bhatia, S.: Nanoparticles types, classification, characterization, fabrication methods and drug delivery applications. In: Natural Polymer Drug Delivery Systems, pp. 33–93. Springer, Cham (2016)
[38]. Mosmann, T.: Rapid colorimetric assay for cellular growth and survival. J. Immunol. Methods 65, 55–63 (1983)
[39]. Chou, T.C.: Theoretical basis, experimental design, and computerized simulation of synergism and antagonism in drug combination studies. Pharmacol. Rev. 58, 621–681 (2006)
[40]. Koch, A., et al.: Establishment of early endpoints in preclinical drug discovery. Nat. Rev. Drug Discov. 4, 649–653 (2005)
[41]. Wang, H., Joseph, J.A.: Quantifying cellular oxidative stress by dichlorofluorescein assay using microplate reader. Free Radic. Biol. Med. 27, 612–616 (1999)
[42]. Wilhelm, S., et al.: Analysis of nanoparticle delivery to tumours. Nat. Rev. Mater. 1, 16014 (2016)
[43]. Rejman, J., et al.: Size-dependent internalization of particles via the pathways of clathrin-and caveolae-mediated endocytosis. Biochem. J. 377, 159–169 (2004)
[44]. Ritger, P.L., Peppas, N.A.: A simple equation for description of solute release: Fickian and non-Fickian release from non-swellable devices. J. Control. Release 5, 23–36 (1987)
[45]. Maeda, H., et al.: Tumor vascular permeability and the EPR effect in macromolecular therapeutics. J. Control. Release 65, 271–284 (2000)
[46]. Low, P.S., Kularatne, S.A.: Folate-targeted therapeutic and imaging agents for cancer. Curr. Opin. Chem. Biol. 13, 256–262 (2009)
[47]. Kelkar, S.S., Reineke, T.M.: Theranostics: combining imaging and therapy. Bioconjug. Chem. 22, 1879–1903 (2011)
[48]. Mukherjee, S., et al.: Green synthesis of metal nanoparticles: applications and limitations. In: Green Metal Nanoparticles, pp. 35–75. Wiley, Hoboken (2018)
[49]. Chen, Q., et al.: Nanoscale theranostics for physical stimulus-responsive cancer therapies. Biomaterials 73, 214–230 (2015)
[50]. Mura, S., et al.: Stimuli-responsive nanocarriers for drug delivery. Nat. Mater. 12, 991–1003 (2013)
[51]. Ventola, C.L.: Progress in nanomedicine: approved and investigational nanodrugs. Pharm. Ther. 42, 742–755 (2017)
[52]. Vamathevan, J., et al.: Applications of machine learning in drug discovery and development. Nat. Rev. Drug Discov. 18, 463–477 (2019)